Sports Ballistics

Christophe Clanet

LadHyX, UMR7646, CNRS, Ecole Polytechnique, 91128 Palaiseau, France;
email: christophe.clanet@ladhyx.polytechnique.fr

Annu. Rev. Fluid Mech. 2015. 47:455–78

First published online as a Review in Advance on September 22, 2014

The *Annual Review of Fluid Mechanics* is online at fluid.annualreviews.org

This article's doi:
10.1146/annurev-fluid-010313-141255

Keywords

aerodynamics, sports physics, knuckleball, pop-up, Tartaglia, Roberto Carlos's spiral, shuttlecock flip, ski jump, size of sports fields

Abstract

This review describes and classifies the trajectories of sports projectiles that have spherical symmetry, cylindrical symmetry, or (almost) no symmetry. This classification allows us to discuss the large diversity observed in the paths of spherical balls, the flip properties of shuttlecocks, and the optimal position and stability of ski jumpers.

1. INTRODUCTION

In 1671, Isaac Newton published his new theory of light and wrote about refraction:

> Then I began to suspect, whether the Rays, after their trajection through the Prisme, did not move in curve lines. And it increased my suspicion when I remembred that I had often seen a Tennis ball, struck with an oblique Racket, describe a curve line. (Newton 1671)

One might be surprised by the unexpected use of the word tennis [1] more than two centuries before the official creation of the sport in England (1874). In fact, we find traces of the term as soon as 1400 (Gillmeister 1998). We can imagine that Newton used the analogy with the sport to provide a mental image of the phenomenon for his readers, who had probably spent more time watching games than observing light.

Apart from analogies, sports also generate original questions in physics: Why is the flight of a tennis ball irregular? Rayleigh (1877) addressed this problem using the Magnus force theory to account for the aerodynamics of spinning spheres. What is the best way to run a race? This question was tackled by Keller (1974) using the variational approach. How many passes before the ball is lost in soccer? Reep & Benjamin (1968) treated this point using a statistical approach.

Here, following the advice of Frohlich (2011), we try to keep the tradition alive and address some questions about the trajectories of sports projectiles (**Figure 1**): Apart from parabolas, what trajectories can be observed with spherical balls (Section 2)? What determines the size of sports fields (Section 2.4.3)? How does one throw a knuckleball (Section 2.4.6)? Why do shuttlecocks flip (Section 3)? What is the optimal position for a ski jumper (Section 4)? What role does the symmetry of the particle play in its trajectory (Sections 3 and 4)? To answer these questions, we regularly make reference to the work of famous pioneers, Mehta (1985) and de Mestre (1990).

2. SPHERICAL BALLS

For a homogeneous spherical ball of mass M and velocity $\mathbf{U}$, the whole problem of the ball's trajectory is to solve the equation of motion:

$$M\frac{d\mathbf{U}}{dt} = \mathbf{F}_G + \mathbf{F}_A(\mathbf{U}), \tag{1}$$

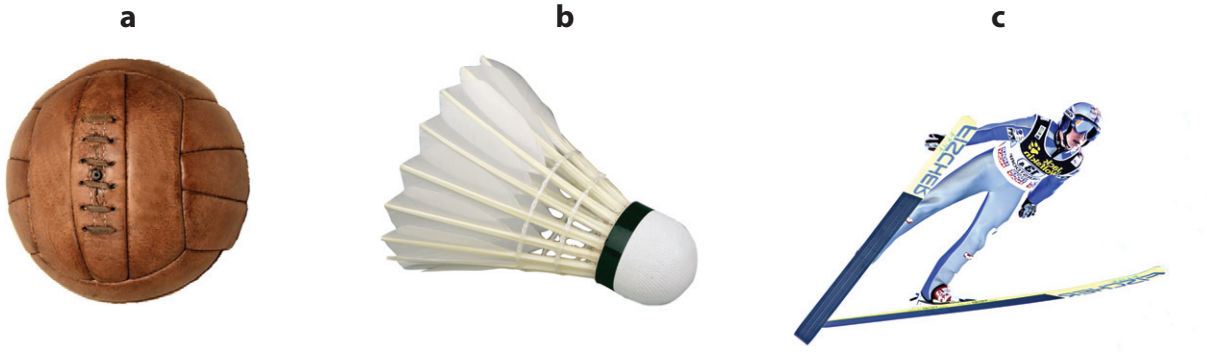

Figure 1

Example of sports projectiles with different symmetries: (*a*) a soccer ball, which has spherical symmetry; (*b*) a shuttlecock, which has cylindrical symmetry; and (*c*) a ski jumper, who has (almost) no symmetry. Photo of Gregor Schlierenzauer by A. Furtner.

[1] The term tennis is from the French *tenez*, which can be translated as "take!", a call from the server to the opponent, indicating that he or she is about to serve.

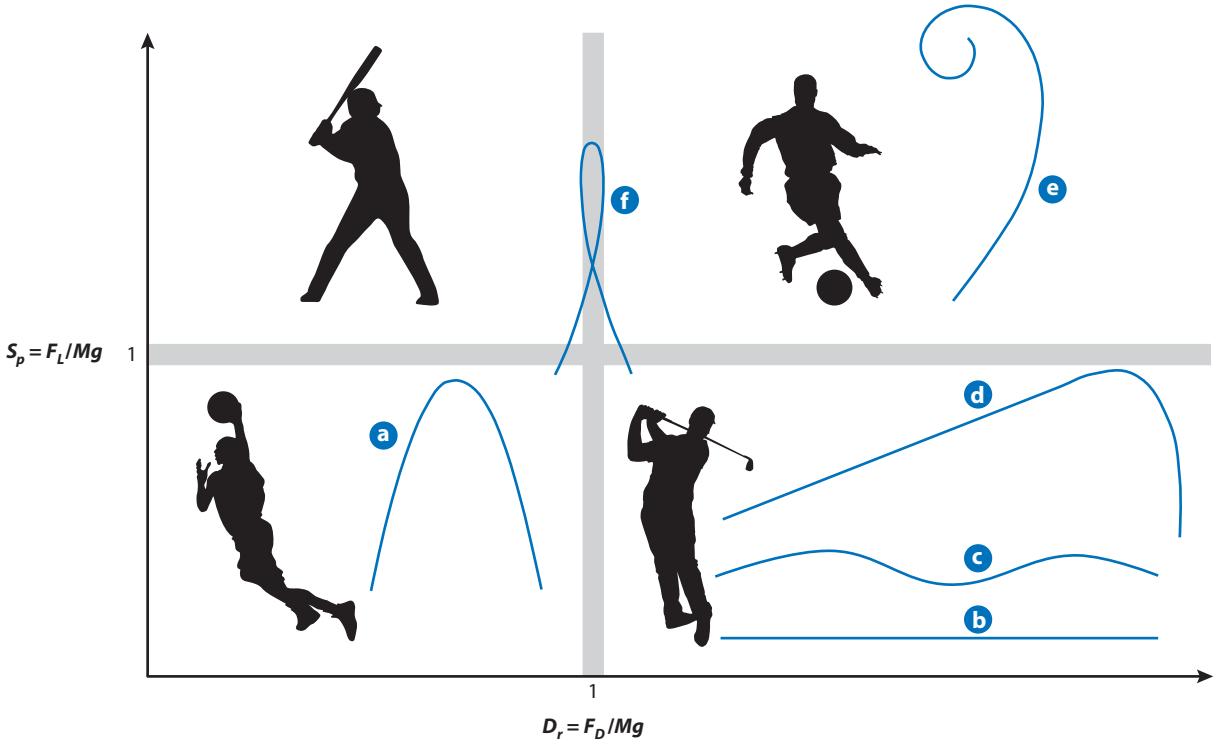

Figure 2

Phase diagram of the different trajectories observed with spheres: (*a*) a parabola, (*b*) straight path, (*c*) knuckleball, (*d*) Tartaglia curve, (*e*) spiral, and (*f*) pop-up.

where $\mathbf{F}_G = M\mathbf{g}$ is the weight, and $\mathbf{F}_A(\mathbf{U})$ is the aerodynamic force. To illustrate the diversity of the ballistic problem, I use the classical drag-lift decomposition of the aerodynamic force, $\mathbf{F}_A = \mathbf{F}_D + \mathbf{F}_L$. In this expression, $\mathbf{F}_D$ stands for the drag (i.e., the part of the force aligned with the velocity), and $\mathbf{F}_L$ stands for the lift (i.e., the part of the force perpendicular to the velocity).

2.1. The Phase Diagram for the Trajectories

The different trajectories of particles submitted to gravity and aerodynamic forces can be discussed in the phase space ($D_r = F_D/Mg$, $S_p = F_L/Mg$) presented in **Figure 2**: When gravity dominates ($D_r \ll 1$, $S_p \ll 1$), the trajectories reduce to parabolas (trajectory a in the figure) (Galilei 1638). At higher velocities and without rotation ($D_r \gg 1$, $S_p \ll 1$), three different kinds of trajectories exist: straight lines (trajectory b), knuckleballs (trajectory c), and Tartaglia curves (trajectory d) (Tartaglia 1537, Cohen et al. 2014a). When the ball spins ($D_r \gg 1$, $S_p \gg 1$), spirals are observed (trajectory e) (Dupeux et al. 2010). Finally, when the three forces are at play, loops (or pop-ups) appear (trajectory f) (McBeath et al. 2008). This section is devoted to the study of these different paths.

2.2. Characteristics of Ball Games

In a more quantitative presentation, **Table 1** lists the different sports considered in this section, along with the size of the ball, $2R$; its mass, M; and two characteristic velocities (the fastest recorded

Table 1 Characteristics of various sports projectiles

Sport	$2R$ (cm)	M (g)	U_{max} (m/s)	U_∞ (m/s)	$Re = 2RU_\infty/\nu$	C_D	$R\Omega_0$ (m/s)	F_D/Mg	F_L/Mg
Badminton	6.0	5.00	137	6.7	3×10^4	0.64	0.019	420	0.1
Tennis	6.5	55.0	73.0	22	1×10^5	0.56	10	11	3
Ping-pong	4.0	2.50	32.0	10	3×10^4	0.36	17	10	18
Squash	4.0	24.0	78.0	34	1×10^5	0.30	3.1	5.4	0.8
Jai alai	6.5	120	83.0	41	2×10^5	0.38	0.20	4.1	0.03
Golf	4.2	45.0	91.0	48	2×10^5	0.23	7.7	3.6	1.4
Volleyball	21	210	37.0	20	4×10^5	0.25	5.3	3.4	2.1
Soccer	21	450	51.0	30	5×10^5	0.24	9.1	2.9	2.3
Softball	9.7	190	47.0	33	3×10^5	0.38	6.1	2.0	0.7
Baseball	7.0	145	54.0	40	2×10^5	0.38	6.6	1.8	0.6
Cricket	7.2	160	53.0	40	3×10^5	0.40	3.4	1.8	0.3
Lacrosse	6.3	143	50.0	48	3×10^5	0.35	0.20	1.1	0.01
Handball	19	450	27.0	36	6×10^5	0.20	0.60	0.56	0.07
Basketball	24	650	16.0	31	6×10^5	0.24	0.75	0.27	0.06

The diameter $2R$ and mass M are extracted from the official rules of the different federations. The sources for the maximum recorded speed U_{max} are as follows: badminton (RIA Novosti 2013; **http://en.wikipedia.org/wiki/Tan_Boon_Heong**), tennis (**http://en.wikipedia.org/wiki/Fastest_recorded_tennis_serves**), ping-pong (Turberville 2003), squash (**http://en.wikipedia.org/wiki/Cameron_Pilley**), jai alai (**http://en.wikipedia.org/wiki/Jai_alai**), golf (**http://en.wikipedia.org/wiki/Golf_ball**), volleyball (Volleywood 2012), soccer (**http://www.guinnessworldrecords.com**), softball (Nathan 2003, Russell 2008, Alam et al. 2012), baseball (eFastball.com 2011, Greenwald et al. 2001), lacrosse (**http://www.guinnessworldrecords.com**), handball (Gorostiaga et al. 2005), and basketball (Huston & Cesar 2003). The terminal velocities, U_∞, have been measured in a vertical wind tunnel (Cohen et al. 2014a). The Reynolds number Re is calculated with an air viscosity of $\nu = 1.5 \times 10^{-5}$ m^2/s. The drag coefficient C_D is linked to the mass and terminal velocity via the relation $C_D = 2Mg/(\rho U_\infty^2 \pi R^2)$. The data for the spin velocity are mainly extracted from Cottey (2002).

speed of the game, U_{max}, and the terminal velocity, U_∞). The table also includes badminton to stress its difference in velocity with the other sports. The terminal velocity is defined as the levitating speed, that is, the speed for which the drag exactly equals the weight, $F_D(U_\infty) = Mg$. The corresponding Reynolds number (Re) is also listed in the table and is found to be of the order of 10^5 for all sports. In this limit, we can write the drag force F_D as

$$\mathbf{F}_D(\mathbf{U}) = -\frac{1}{2}\rho U\,\mathbf{U} S C_D, \tag{2}$$

where ρ is the density of air, $S = \pi R^2$ is the cross-sectional area of the ball, and C_D is the drag coefficient. For the different sports, **Table 1** lists the drag coefficient at the terminal velocity and presents the maximal recorded spinning velocity ($R\Omega_0$), prior to the calculation of the reduced drag, $D_r = F_D/Mg$, and reduced lift, $S_p = F_L/Mg$. It is classical to use a formula similar to Equation 2 to calculate the lift: $F_L = 1/2\rho U^2 S C_L$. However, this formulation does not allow one to determine the direction of the force and the link with the rotation of the ball. We thus use a different expression for the lift, based on the Blasius formula:

$$\mathbf{F}_L(\mathbf{U}) = \rho R^3 \boldsymbol{\Omega} \wedge \mathbf{U} C_\Omega, \tag{3}$$

where $\boldsymbol{\Omega}$ is the spin vector and C_Ω the spin coefficient. Using data from Nathan (2008), we evaluate $C_\Omega \approx 1.7$ in the range $R\Omega_0/U < 0.5$, which holds for all the sports listed in **Table 1**. Equation 3 can be used to compare the lift force to the weight in the table. A deeper discussion on the Magnus effect in ball games can be found in the work of Bush (2013).

2.3. Classification of Ball Games

With reduced drag and reduced lift, each sport listed in **Table 1** is positioned in the phase diagram (D_r, S_p) in **Figure 3**. This presentation reveals several striking features: Basketball and handball are two gravitational sports for which aerodynamics plays no role on the ball's trajectory. Only parabolas are expected to be observed. Spin is used, but only for bouncing purposes, not for flight control. Another consequence is that these sports are not sensitive to wind and can be practiced outdoors without perturbation. The conclusion is exactly the opposite for badminton, for which the drag can be as large as 400 times the weight. In this classification, the more complete aerodynamic sport appears to be ping-pong, in the sense that both the drag and lift are of the order of 10 times the weight. Between these extremes, we observe a large concentration of sports in the region (1, 1). This is probably not a coincidence as this is the region where all the effects (drag, lift, gravity) can be used to increase the diversity (and perhaps the interest) of sport balls' trajectories.

2.4. The Different Trajectories

The previous discussion shows that the equation of motion for balls (Equation 1) can be written as

$$M\frac{d\mathbf{U}}{dt} = M\mathbf{g} - \frac{1}{2}\rho U\,\mathbf{U}SC_D + \rho R^3\boldsymbol{\Omega}\wedge\mathbf{U}C_\Omega. \tag{4}$$

This equation does not admit a general analytic solution, and it thus reduces the analysis to several asymptotic regimes.

2.4.1. The parabola. The first regime concerns basketball and handball, for which gravity dominates both the drag and lift ($D_r \ll 1$, $S_p \ll 1$). **Figure 4*a*** presents an example of a basketball's trajectory. In this limit, Equation 4 reduces to $d\mathbf{U}/dt = \mathbf{g}$, which implies that the particle never reaches a steady state (defined by a constant $\mathbf{U}$). As first noticed by Galileo (**Figure 4*b***), the particle follows the parabolic path:

$$y = \tan\theta_0\, x - \frac{g}{2U_0^2\cos^2\theta_0}x^2, \tag{5}$$

where θ_0 is the initial angle with the horizontal direction, and y is the vertical height. This path presents a left-right symmetry with respect to the maximum location ($y_{\max} = U_0^2\sin^2\theta_0/2g$) and returns to the ground at the range $x_0 = U_0^2\sin 2\theta_0/g$ defined by $y(x_0) = 0$.

2.4.2. Tartaglia curves. The next regime concerns sports located in the bottom right corner of the phase diagram in **Figure 3** ($D_r \gg 1$, $S_p \ll 1$) for which badminton is a paradigm. **Figure 5*a*** presents an example of a shuttlecock path. Here, the left-right symmetry is broken, and the particle seems to reach a steady state with a negative vertical velocity. Because $S_p \ll 1$, the lift can be neglected, and the equation of motion (Equation 4) reduces to

$$M\frac{d\mathbf{U}}{dt} = M\mathbf{g} - \frac{1}{2}\rho U\,\mathbf{U}SC_D. \tag{6}$$

This equation indeed allows a steady state ($d\mathbf{U}/dt = \mathbf{0}$) when the two terms on the right-hand side balance each other. In this steady state, the drag exactly balances the weight, and the velocity is aligned with gravity, taking its levitating value: $\mathbf{U} = -U_\infty\mathbf{e}_y$, with $U_\infty = \sqrt{2Mg/\rho SC_D}$. For badminton, this terminal velocity is 6.7 m/s, a value close to the one that can be measured in

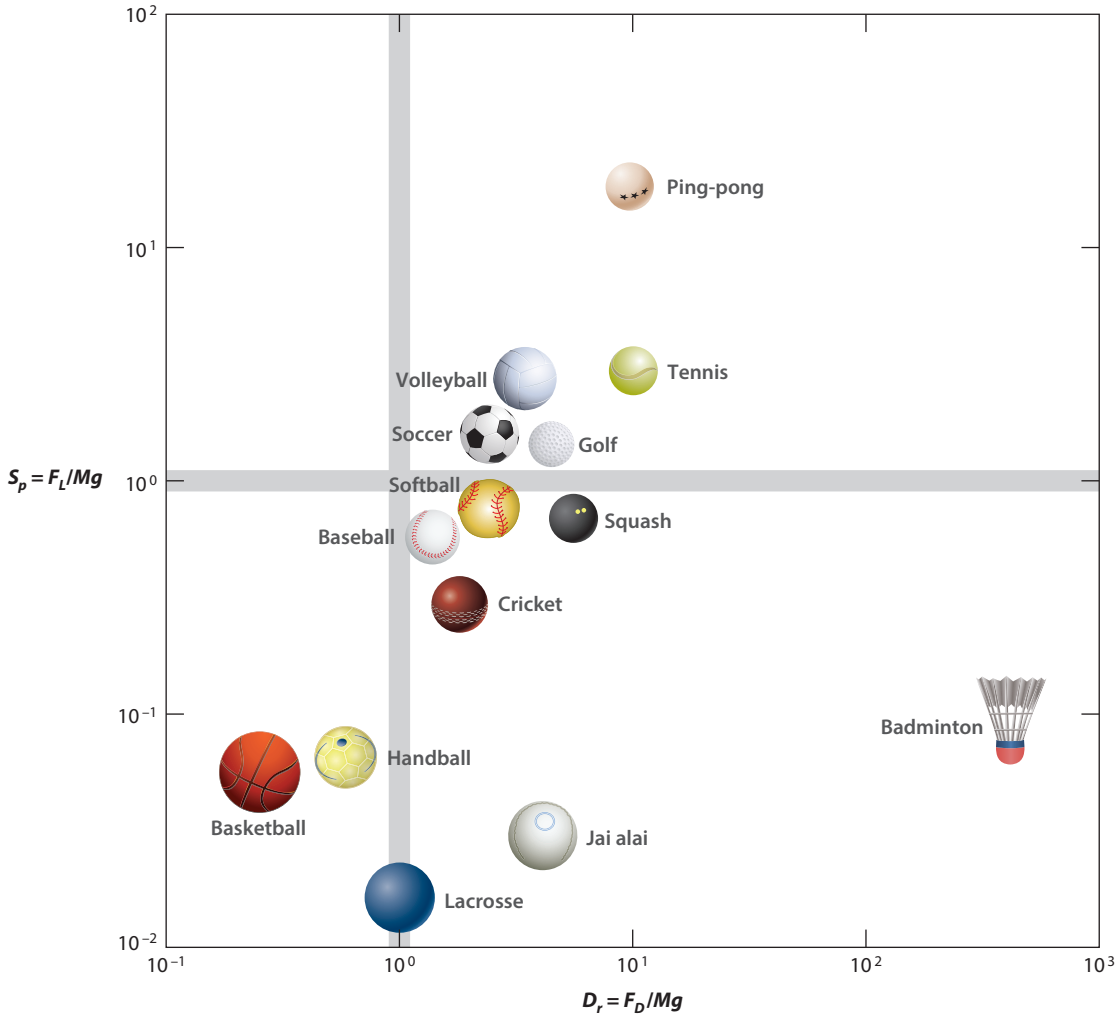

Figure 3

Position of the different sports presented in **Table 1** in the phase diagram (D_r, S_p).

Figure 5*a* when the shuttlecock returns to the ground. This terminal regime is illustrated with a vertical asymptote in **Figure 5*b*** and is referred to as regime 3.

However, the velocity of the particle, $U_0 = 59$ m/s, is initially much larger than U_∞, and the drag is thus initially much larger than the weight. This implies that the initial path of the particle simply results from a balance between inertia and drag, $Md\mathbf{U}/ds = -1/2\rho\mathbf{U}SC_D$, where the relation $U = ds/dt$ is used to switch from the time to space derivative (s is the curvilinear location of the particle). Because the drag force is aligned with the velocity, there is no lateral deviation, and the particle follows a straight line with an exponentially decreasing velocity: $\mathbf{U}(s) = \mathbf{U}_0\, e^{-s/\mathcal{L}}$, with $\mathcal{L} = 2M/\rho SC_D = U_\infty^2/g$. This characteristic length depends only on the ball properties (M, $S = \pi R^2$, C_D) and fluid density. For badminton, using the data presented in **Table 1**, we find $\mathcal{L} = 4.6$ m. A straight path with a velocity that decreases exponentially over a characteristic length

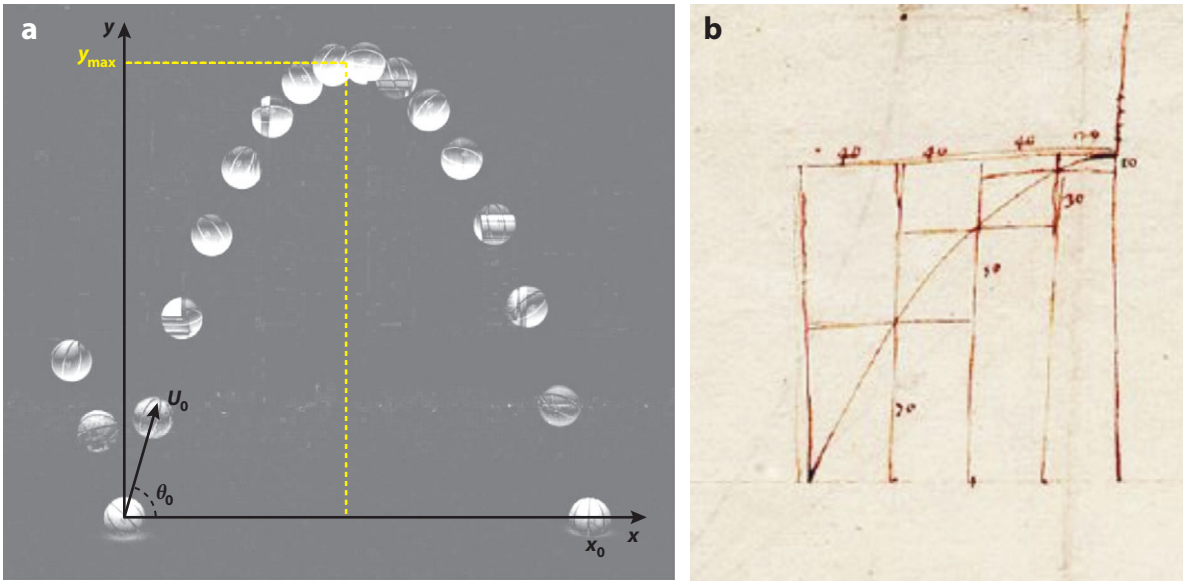

Figure 4

(*a*) Chronophotography of a basketball's path obtained with the values $\theta_0 = 73°$ and $U_0 = 6.5$ m/s and a time step between images of $\Delta t = 90$ ms. Panel *a* adapted with permission from Darbois-Texier (2013). (*b*) Drawing of the parabola discussed in theorem 1 of the fourth day of *Two New Sciences*, reproduced from Galilei (1638). Complementary information can be found in Drake (1973).

scale of 4.6 m is compatible with what is observed in **Figure 5*a***. This initial regime is illustrated with an inclined asymptote of slope θ_0 in **Figure 5*b*** and is referred to as regime 1. The inertia-drag balance is thus replaced at long times by a gravitational-drag equilibrium. Between these two asymptotic regimes, the three terms in Equation 6 connect these two straight line regimes and account for the turn (regime 2 in **Figure 5*b***). Importantly, during the whole path of the particle, drag is always involved, which means that the balance $d\mathbf{U}/dt = \mathbf{g}$ is never achieved. Because this balance is responsible for the parabola, we must conclude that the trajectory of a shuttlecock is never a parabola. We call it a Tartaglia curve as this type of path was first reported by Tartaglia (1537) in the context of artillery, one century before Galileo's work (**Figure 5*c***).

Here, we conclude that for a given particle, two characteristic velocities (U_0 and U_∞) are needed to predict the shape of the trajectory. If $U_0 < U_\infty$, the drag is initially smaller than the weight, and a parabola is observed. However, if $U_0 > U_\infty$, the drag always matters, and one observes a Tartaglia curve. Considering the data in **Table 1**, we notice that for all sports except basketball and handball, a Tartaglia curve is observed at the highest speed.

Concerning the range of a particle released without spin, Cohen et al. (2014a) recently presented a detailed calculation that extends previous theoretical discussions and numerical solutions (Lamb 1914, Erlichson 1983, de Mestre 1990, Chudinov 2010). It yields the following approximate analytical expression:

$$x_0 = \frac{1}{2}\mathcal{L}\cos\theta_0 \ln\left[1 + 4\left(\frac{U_0}{U_\infty}\right)^2 \sin\theta_0\right]. \qquad (7)$$

At low velocities ($U_0 < U_\infty$), this expression reduces to the parabolic range, $x_0 = U_0^2 \sin(2\theta_0)/g$. In the opposite limit ($U_0 > U_\infty$), we find a logarithmic saturation. Applying this formula to the

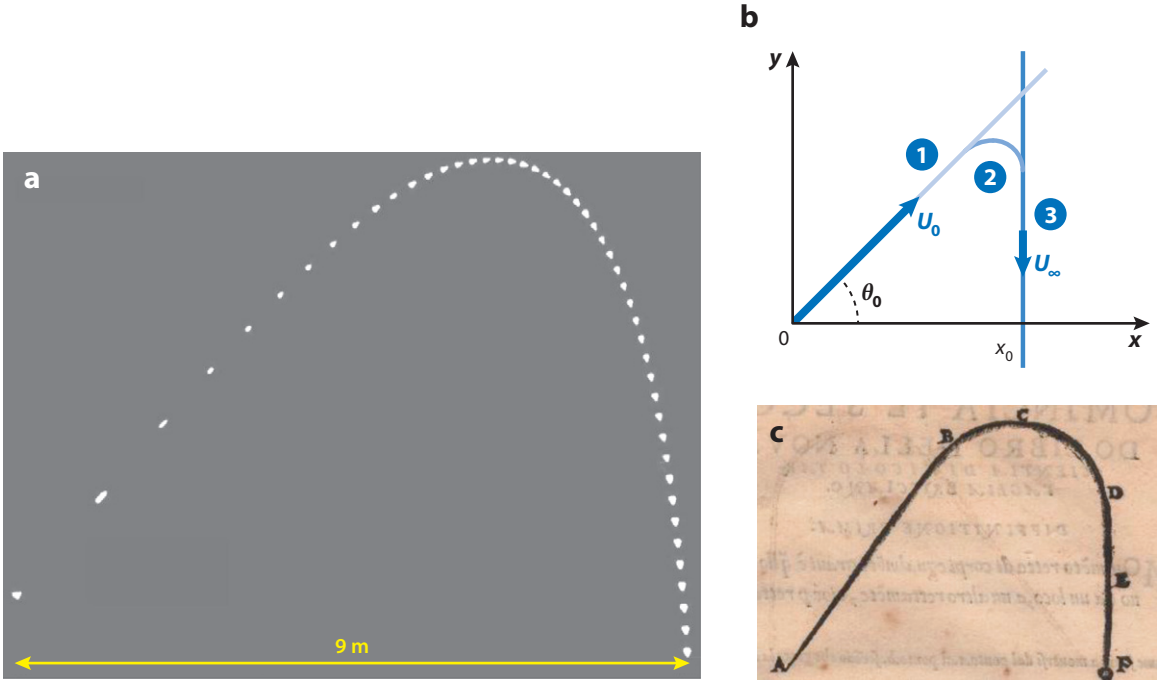

Figure 5

(*a*) Chronophotography of a shuttlecock's path obtained with the values $\theta_0 = 52°$ and $U_0 = 59$ m/s and a time step between images of $\Delta t = 50$ ms. With the first two tracks, the image shows 40 m/s, but the shuttlecock has already decelerated. Panel *a* adapted with permission from Darbois-Texier et al. (2014). (*b*) Schematic illustration of the asymptotic regimes of a Tartaglia curve. (*c*) Illustration of a bullet path from the treatise *Nova Scientia*. Panel *c* reproduced from Tartaglia (1537).

trajectory presented in **Figure 5*a***, we get $x_0 \approx 8.5$ m, which is compatible with the observed range. For comparison, the parabolic range in this case is $U_0^2 \sin(2\theta_0)/g \approx 244$ m.

From Equation 7, the optimal angle, $\theta_{\max}$, that maximizes the range and the corresponding maximum range $x_{\max} = x_0(U_{\max}, \theta_{\max})$ can be calculated as

$$x_{\max} = \frac{1}{2}\mathcal{L}\cos\theta_{\max}\ln\left[1 + 4\left(\frac{U_{\max}}{U_\infty}\right)^2 \sin\theta_{\max}\right], \tag{8}$$

with

$$\theta_{\max} = \arctan\sqrt{\frac{(U_{\max}/U_\infty)^2}{[1+(U_{\max}/U_\infty)^2]\ln[1+(U_{\max}/U_\infty)^2]}}. \tag{9}$$

In the limit $U_{\max}/U_\infty \ll 1$, Equation 8 reduces to $x_{\max} = 2U_{\max}^2/g \sin\theta_{\max}\cos\theta_{\max}$, whereas Equation 9 leads to $\theta_{\max} = \arctan(1)$. We thus recover the parabolic regime in which the range is maximized with $\theta_{\max} = \pi/4$ and takes the value $x_{\max} = U_{\max}^2/g$. In the opposite limit in which $U_{\max}/U_\infty \gg 1$, the maximal value of the range weakly increases with the velocity while the optimal angle decreases, as studied by Cohen et al. (2014a). What is important to realize is that once the velocities $U_{\max}$ and U_∞ are known, the problem of the maximal range is solved, as Equation 9 provides the optimal angle and Equation 8 provides the maximal range $(\mathcal{L} = U_\infty^2/g)$. In sports, U_∞ is fixed by the choice of the ball (shape and mass), and $U_{\max}$ is fixed by the launch method (e.g., throw, bat, racket, kick).

Table 2 The size of the ball ($D = 2R$), the length of the sports field (L_{field}), the density of the ball (ρ_s), the wavelength λ calculated with Equation 17 using $C_{Lm} = 0.2$ (λ), the length ratio (L_{field}/λ), and the critical Reynolds number (Re_c) for various sports

Sport	$D = 2R$ (m)	L_{field} (m)	ρ_s (kg/m^3)	λ (m)	L_{field}/λ	Re_c	Re_{max}/Re_c
Badminton	6.0	13.4	44.21	4.18	3.2	No	No
Tennis	6.5	24.0	382.5	13.3	1.8	No	No
Ping-pong	4.0	2.70	74.60	3.62	0.75	4.0×10^5	0.21
Squash	4.0	9.75	716.2	11.2	0.87	4.0×10^5	0.52
Jai alai	6.5	54.0	834.5	19.7	2.7	1.3×10^6	0.28
Golf	4.2	225	1,160	15.0	15	4.0×10^4	6.4
Volleyball	21	18.0	43.31	14.5	1.2	1.7×10^5	3.0
Soccer	21	100	92.80	21.2	4.7	1.5×10^5	4.8
Softball	9.7	76.0	397.6	20.3	3.8	1.3×10^5	2.3
Baseball	7.0	110	807.4	20.8	5.3	1.3×10^5	1.9
Cricket	7.2	160	818.7	21.6	7.4	1.3×10^5	2.0
Lacrosse	6.3	100	1,067	21.7	4.6	4.0×10^5	0.53
Handball	19	40.0	125.3	22.3	1.8	3.5×10^5	0.98
Basketball	24	28.0	89.80	23.8	1.2	3.5×10^5	0.73

For golf, volleyball, and baseball, the values have been extracted from the work of Mehta (2008). For soccer, data are from Asai et al. (2007). For ping-pong, squash, and lacrosse, we take the values corresponding to a smooth sphere (Mehta & Pallis 2001). For badminton (Cooke 1999) and tennis (Mehta et al. 2008), no drag crisis has been observed. Owing to ball similarity (and lack of available data on the drag crisis), we assume that softball and jai alai have the same characteristics as baseball. For the same reason, the values for handball and basketball have been assumed to be close to that for a smooth sphere. The ratio between the maximal value of the Reynolds number, Re_{max}, and the critical Reynolds number, Re_c, is shown in the last column.

2.4.3. The size of sports fields. Darbois-Texier et al. (2014) developed the following argument to understand the link between the maximal range of the ball and the size of a sports field: If we consider the example of two opponents playing with a soft balloon, the common experience is that regardless of the strength of the hit, the range of the balloon never exceeds $x_{max} = 3$ m. Now let us imagine that the sports field is 100 m long with a net at the center: We expect the players to stay close to the net in a region of the order of the range. We thus anticipate the useful sports field size to be comparable to the range. More generally, it is natural to compare the maximum projectile range deduced from Equations 8 and 9 with the corresponding field length, L_{field}, given in **Table 2**. **Figure 6** plots the size of the field, L_{field}, for each sport as a function of the associated ball's maximal range, x_{max}. The equality $L_{field} = x_{max}$ is underlined with the solid line. It is remarkable that, without any free parameter to calculate x_{max}, we observe a strong correlation between the maximal range and the field dimensions. This correlation implies that once a ball is chosen, one is able to calculate U_∞, and knowing U_{max} (from the way the ball is launched), it is then possible via Equations 8 and 9 to predict the size of the field on which this game should be played. Despite the strong correlation between L_{field} and x_{max}, we also observe some deviations in **Figure 6** that are further discussed in Darbois-Texier et al. (2014).

2.4.4. Roberto Carlos's spiral. Roberto Carlos scored a wonder goal during the inaugural match of the Tournoi de France, a friendly international soccer tournament held in France a year before the 1998 World Cup. **Figure 7*a*** presents the free kick location and the ball's path. Roberto Carlos kicked the ball with the external side of his left foot, which led to an anticlockwise spin of the ball of the order of $\Omega_0 = 88$ rad/s (Dupeux et al. 2011). The velocity is close to 40 m/s, well

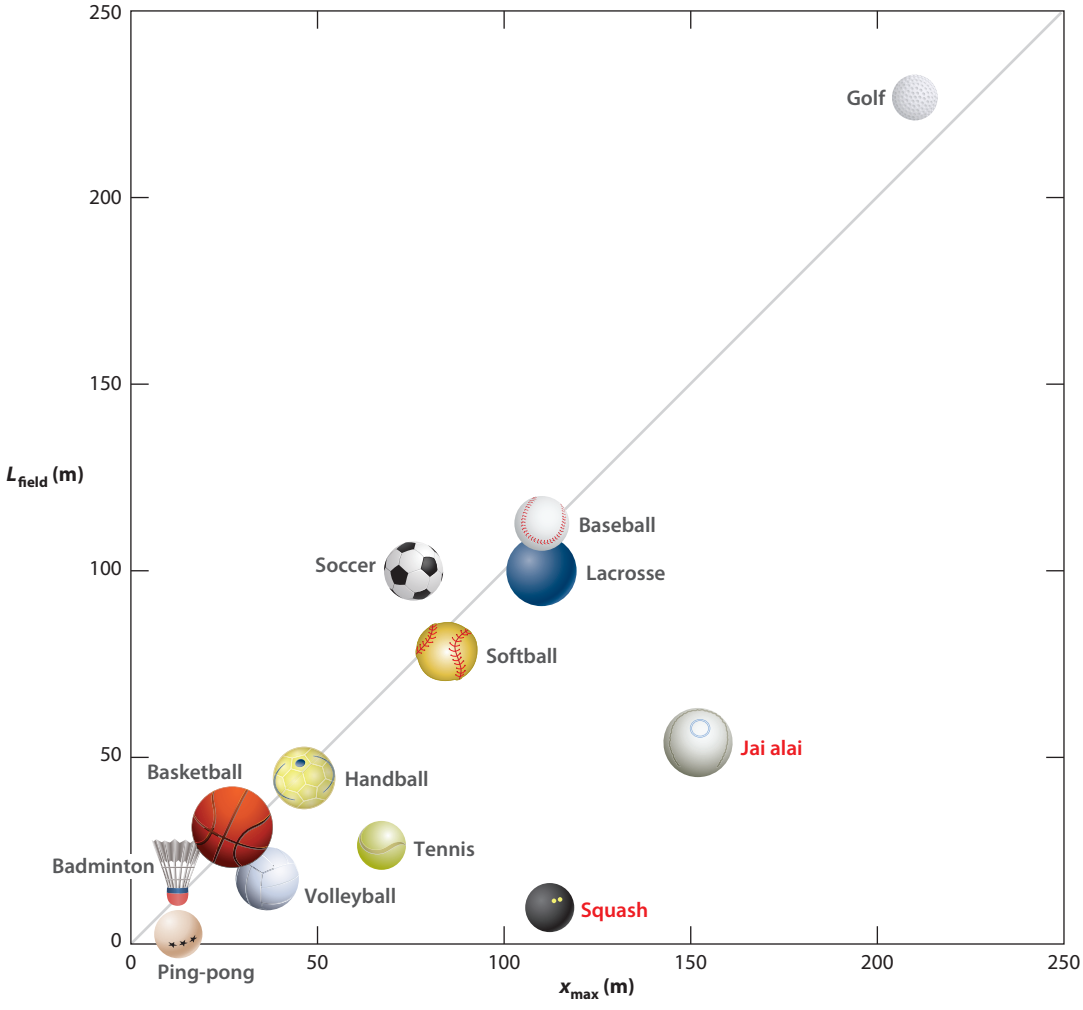

Figure 6

Correlation between the size of different sports fields (L_{field}) and the associated maximum range of the corresponding ball (x_{max}). The data are taken from **Tables 1** and **2**. The solid line represents the equality between the two distances. Red labels indicate games that are played on a closed field or court. Figure adapted with permission from Darbois-Texier et al. (2014).

above the levitating speed ($U_\infty = 30$ m/s in **Table 1**). To analyze the path of the ball and stress its specificity, we consider the limit in which both the drag and lift matter and gravity can be neglected ($D_r \gg 1$, $S_p \gg 1$). Experimentally, this limit has been studied in water with isodensity spinning spheres by Dupeux et al. (2010). **Figure 7*b*** presents one of their chronophotographs, revealing a spiral path of the particle. To analyze the trajectory, we write the equation of motion (Equation 4) in the zero-gravity limit and use the Frenet-Serret coordinate system ($\mathbf{t}, \mathbf{n}, \mathbf{b} = \mathbf{t} \wedge \mathbf{n}$) presented in **Figure 7*b***:

$$MU\frac{d\mathbf{U}}{ds}\mathbf{t} + MU^2\frac{d\theta}{ds}\mathbf{n} = -\frac{1}{2}\rho U^2 S C_D \mathbf{t} + \rho R^3 \Omega_0 U C_\Omega \mathbf{n}. \quad (10)$$

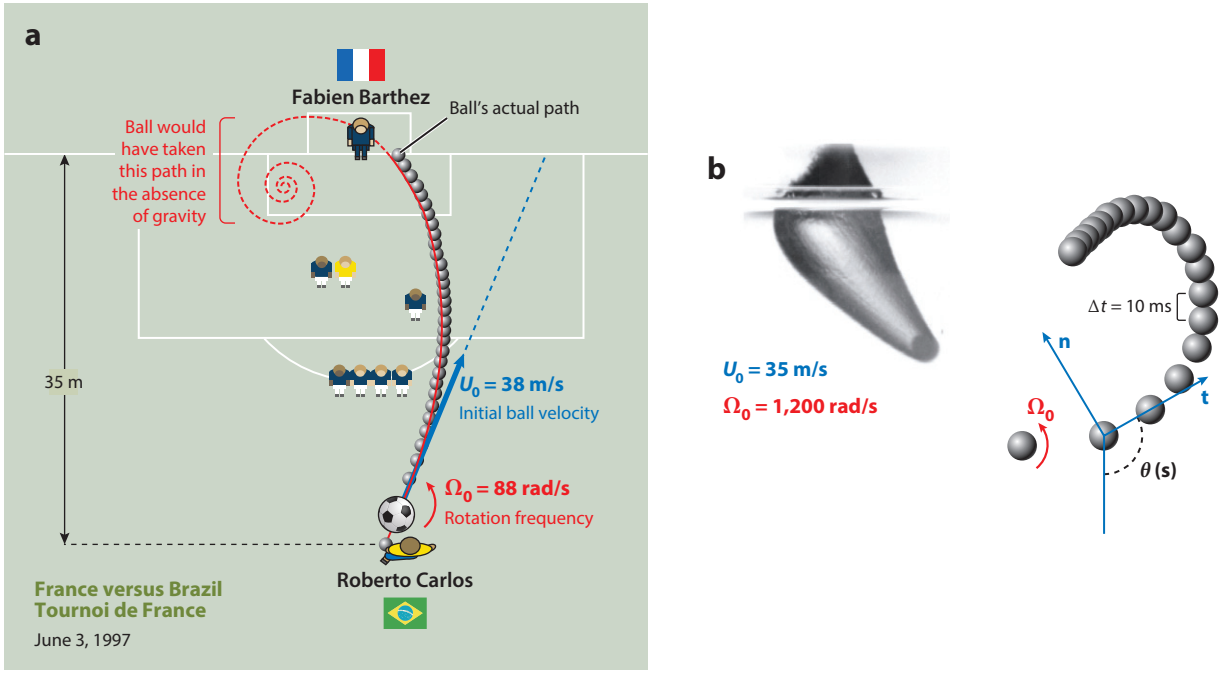

Figure 7

(*a*) Scheme of Roberto Carlos's wonder goal scored against France on June 3, 1997. The initial ball velocity is $U_0 = 38$ m/s, and the rotation frequency is $\Omega_0 = 88$ rad/s (Dupeux et al. 2011). (*b*) Multipose image showing the trajectory of an isodensity sphere ($R = 3.5$ mm) penetrating a bath of water at $U_0 = 35$ m/s and spinning at $\Omega_0 = 1{,}200$ rad/s. The time step between successive ball locations is $\Delta t = 10$ ms. This image reveals a spiral trajectory. Figure reproduced with permission from Dupeux et al. (2010).

This equation is derived assuming that $\mathbf{\Omega} = \Omega_0\,\mathbf{b}$, which means that the spin vector is normal to the plane containing the trajectory. In this limit, the projection of Equation 10 along the **t** direction leads to $MU\ dU/ds = -\rho U^2 S C_D/2$, which implies $U(s) = U_0 e^{-s/\mathcal{L}}$. Along the **n** direction, the equation reduces to $MU^2 d\theta/ds = \rho R^3 \Omega_0 U C_\Omega$. Using the expression of the velocity $U(s)$, we get

$$\frac{d\theta}{ds} = \frac{1}{\mathcal{L}_S}\, e^{s/\mathcal{L}} \quad \text{with} \quad \mathcal{L}_S = \frac{4\pi}{3C_\Omega}\,\frac{\rho_s}{\rho}\,\frac{U_0}{\Omega_0}. \tag{11}$$

The curvature is initially $1/\mathcal{L}_S$ (Truscott & Techet 2009) and then increases exponentially over the characteristic length $\mathcal{L}$, provided the rotation rate Ω_0 remains constant (Dupeux et al. 2010).

As far as sports are concerned, an important property of the spiral is the distance, D_S, between the impact and the center of the spiral at which the ball is expected to finish its trajectory (**Figure 8**). Numerically, we find $D_S = \mathcal{L} \cdot \ln(1 + \mathcal{L}_S/\mathcal{L})$. For soccer, the values in **Table 1** lead to $\mathcal{L} \approx 90$ m. Using the data corresponding to Roberto Carlos's free kick ($U_0 = 38$ m/s, $\Omega_0 = 88$ rad/s), we find $\mathcal{L}_S = 82$ m so that $D_S \approx 58$ m. Roberto Carlos's spiral is thus characterized by two length scales: the initial radius of curvature, $\mathcal{L}_S$, and the location of the whirling, D_S. For shot distances, d, smaller than these two sizes, one cannot distinguish the ball's trajectory from a straight line. The soccer players thus never use spin for penalty shots ($d = 11$ m; **Figure 8*a***). As the shot distance increases, a larger portion of the spiral is revealed, which is close to a circle of radius $\mathcal{L}_S$ (**Figure 8*b***). At even larger shot distances, the increase of the curvature becomes sensitive and can surprise

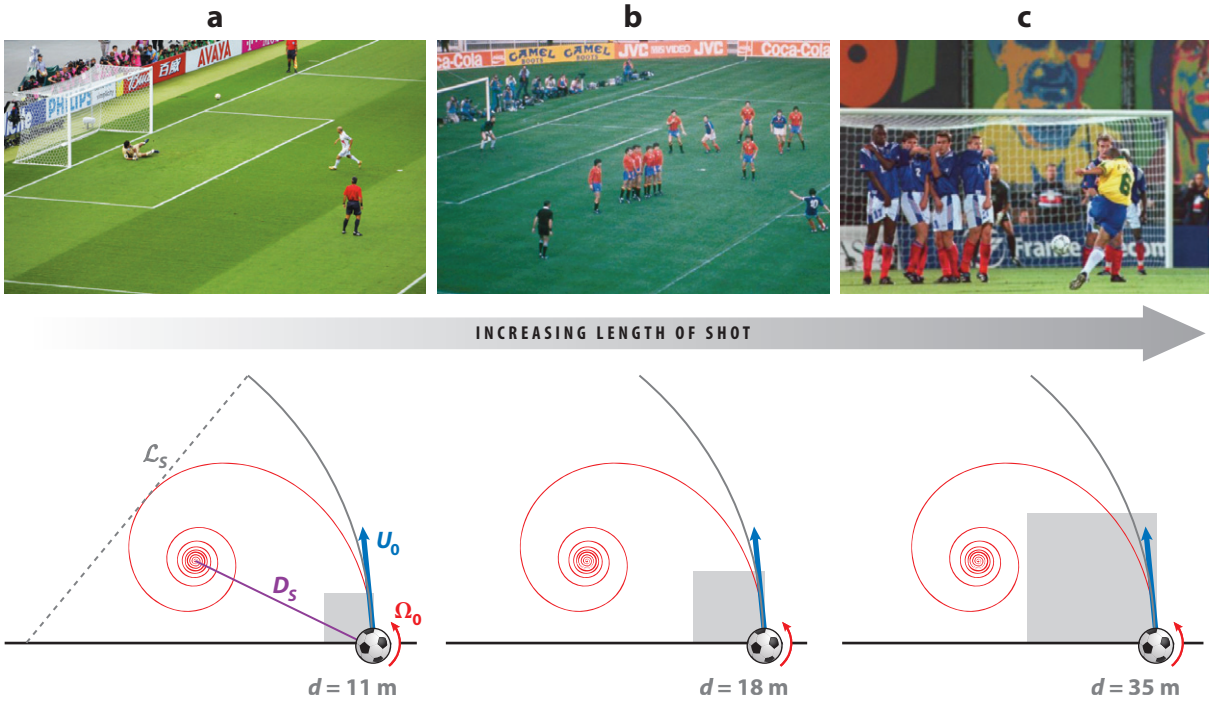

Figure 8

Three kinds of shots in soccer: (*a*) Zinedine Zidane's Panenka shot in 2006 against Italy, (*b*) Michel Platini's free kick during Euro 1984 against Spain, and (*c*) Roberto Carlos's free kick in 1997 against France. Panel *a* courtesy of Michael Bryan, panel *b* courtesy of Panoramic, and panel *c* courtesy of the Press Association.

goalkeepers (**Figure 8*c***). This spiral is obviously not specific to soccer, and the same path can be observed in ping-pong during forehand smashes or in tennis during fast topspin.

2.4.5. The paradoxical pop-ups. A pop-up in baseball is a batted ball hit very high that stays in the infield. Usually these balls are easy to catch, and thus the batter is out. However, with large slice, these balls become very difficult to catch, even for major league infielders (**Figure 9*a***). McBeath et al. (2008) have shown that in this case, the trajectory follows a nonparabolic flight with unexpected behaviors around the apex, such as a cusp and loop. A simplified version of their complete analysis is derived below to stress the conditions that are compulsory to enter this paradoxical regime.

Even if the spin can alter a baseball's trajectory, **Table 1** clearly shows that gravity always matters. The equation for the trajectory is thus described by the full equation

$$M\frac{d\mathbf{U}}{dt} = -Mg\mathbf{e}_y - \frac{1}{2}\rho U^2 S C_D \mathbf{t} + \rho R^3 \Omega_0 U\, C_\Omega \mathbf{n}. \qquad (12)$$

Because pop-ups are quasi-vertical trajectories, this implies that the tangent $\mathbf{t}$ and normal $\mathbf{n}$ vectors satisfy $\mathbf{t}\cdot\mathbf{e}_x \approx \mathbf{0}$ and $\mathbf{n}\cdot\mathbf{e}_y \approx \mathbf{0}$. Along the $\mathbf{e}_x$ direction, Equation 12 thus reduces to $M\,dU_x/ds = -\rho R^3 \Omega_0 C_\Omega dy/ds$. This equation can be integrated once as $dx/dt = -\rho R^3 \Omega_0 C_\Omega y(t)/M$. Now along the $\mathbf{e}_y$ direction, the two main forces are the weight and the drag. McBeath et al. (2008) worked with the value $D_r = F_D/Mg \approx 0.3$. We thus assume that gravity dominates the drag, which reduces Equation 12 to $dU_y/dt = -g$. The height of the ball thus follows the temporal

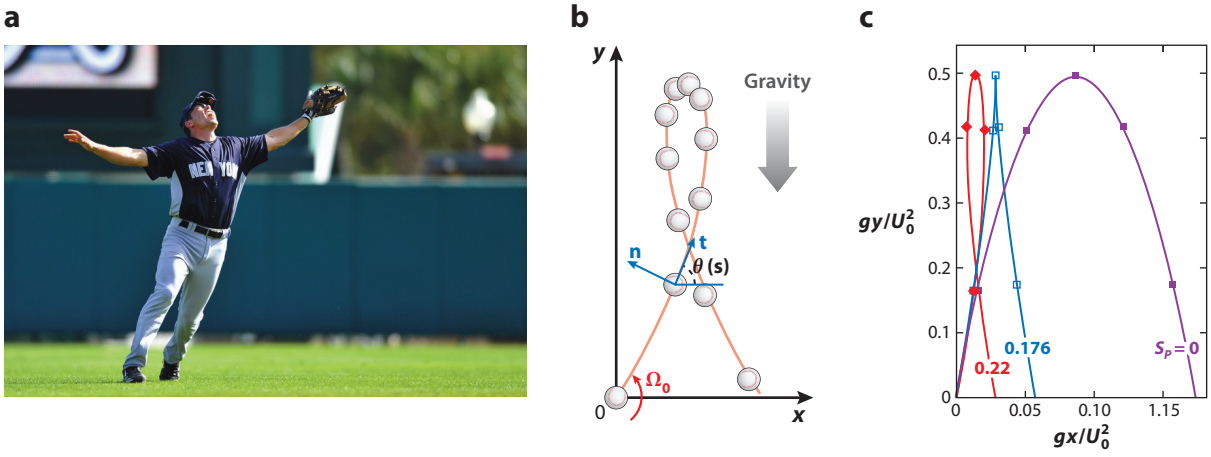

Figure 9

(*a*) New York Yankees infielder Doug Bernier calls for an infield pop-up during a spring training game against the Atlanta Braves at Champion Park in Orlando, Florida, on March 8, 2011. The Yankees edged out the Braves 5 to 4 in Grapefruit League action. Panel *a* courtesy of Ed Wolfstein Photo. (*b*) Conventions used to describe the pop-up. (*c*) Parametric curves obtained using Equations 13 and 14 plotted with $\theta_0 = 85°$ and different values of the lift to weight ratio: $S_p = 0$ (*purple filled squares*), $S_p = 0.176$ (*blue open squares*), and $S_p = 0.22$ (*red diamonds*).

evolution $y(t) = U_0 \sin\theta_0 t - gt^2/2$. From this equation, we integrate the equation for x and get the parametric set of equations:

$$\frac{gx(t)}{U_0^2} = \cos\theta_0 \frac{gt}{U_0} - \frac{1}{2}\sin\theta_0 S_p \left(\frac{gt}{U_0}\right)^2 + \frac{1}{6} S_p \left(\frac{gt}{U_0}\right)^3 \quad \text{with} \quad S_p = \frac{\rho R^3 \Omega_0 U_0 C_\Omega}{Mg}, \tag{13}$$

$$\frac{gy(t)}{U_0^2} = \sin\theta_0 \frac{gt}{U_0} - \frac{1}{2}\left(\frac{gt}{U_0}\right)^2. \tag{14}$$

With no spin ($S_p = 0$), we recover the classical parabolic limit. As the spin increases, the second and third terms on the right-hand side of Equation 13 increase, revealing the cubic evolution of $x(t)$. A cusp forms when the velocity close to the apex becomes vertical. The condition $U_x(y_{\max}) = 0$ leads to the following condition for cusp formation:

$$S_p^\star = \frac{2\cos\theta_0}{\sin^2\theta_0}. \tag{15}$$

A cusp is thus observed when the ratio of the Magnus force to the weight is equal to the critical value $S_p^\star$, which depends on the initial angle. For a quasi-vertical shot ($\theta_0 \to \pi/2$), this value vanishes, and the cusp is easily observed. In the opposite limit of a horizontal shot ($\theta_0 \to 0$), the value of the critical spin (Equation 15) diverges, and no cusp can be observed. When the spin number S_p overcomes the critical value $S_p^\star$, loops are expected. **Figure 9*c*** illustrates these different regimes, with parametric curves obtained with Equations 13 and 14 using the value $\theta_0 = 85°$ and for different values of S_p. One indeed observes a cusp for $S_p = S_p^\star = 2\cos(85)/\sin^2(85) = 0.176$ and a loop for $S_p = 0.22$.

2.4.6. Knuckleballs. A knuckleball is a baseball pitch thrown with the knuckles (**Figure 10*a***) that can produce erratic, unpredictable motion (**Figure 10*b***). Nathan (2012) has discussed what we know about the necessary conditions for observing this erratic motion: "The knuckleball is

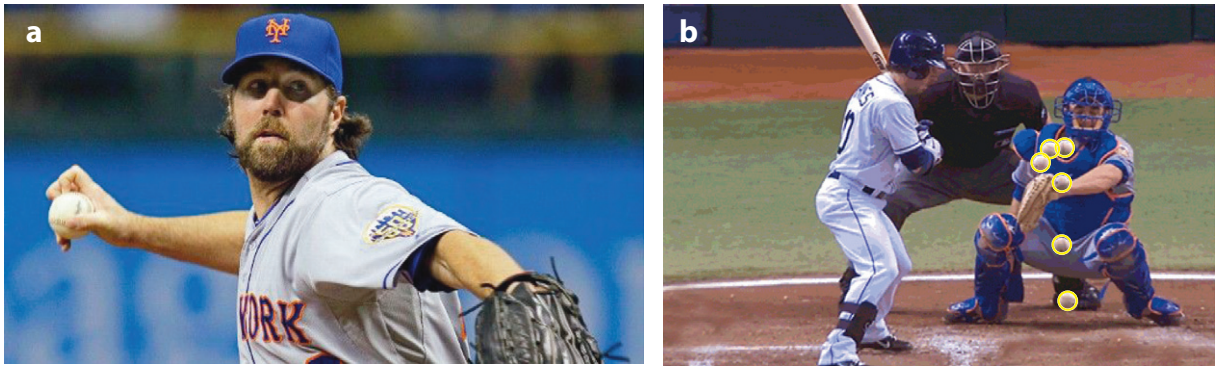

Figure 10

(*a*) R.A. Dickey throwing a knuckleball. Panel *a* courtesy of AP Photo/Chris O'Meara. (*b*) Tracking R.A. Dickey's knuckleball with an effect known as StroMotion from an at bat on June 18, 2013. Panel *b* courtesy of Sheppard (2013).

perhaps the most mysterious of baseball pitches. It is thrown at a speed significantly lower than that of other pitches and with very little spin." There are very few players able to throw such balls. At the moment, R.A. Dickey is the only active major league knuckleball pitcher, and he typically throws balls in the range of 32–34 m/s. Tim Wakefield, who played in the major league from 1992 until 2012, threw knuckleballs at 30 m/s. These velocities are far from the fastest recorded pitch, by Aroldis Chapman (nicknamed the Cuban Missile), 47 m/s (in 2010).

Zigzagging paths also exist in cricket, and the seams on the balls have long been suspected to play a major role in knuckleballs (Mehta 1985, Higuchi & Kiura 2012). However, such erratic trajectories are reported in soccer (Asai & Kamemoto 2011) and in volleyball (Cho 2004, MacKenzie et al. 2012), sports for which balls no longer have seams. For all these sports, the stigmatas remain the same: almost no rotation and a fixed velocity that depends on the sport. Above, we underline that in baseball, the knuckleball velocity lies between 30 and 34 m/s. In volleyball, the velocity for a float serve is between 16 and 18 m/s (Deprá et al. 1998, Häyrinen et al. 2007), and in soccer, knuckleballs are reported in the range of 28 to 36 m/s (Barber et al. 2009, Asai & Kamemoto 2011).

Figure 11*b*,*d* presents a typical knuckleball in soccer. In **Figure 11*b***, the ball moves from left to right, and the use of titanium powder allows the visualization of both the trajectory and the vortex structures in the wake. Usually, a soccer ball at high velocities goes straight, as in **Figure 11*a***. However, in some special cases, it deviates from a straight line and exhibits sidewise motion of several ball diameters. The length scale of the zigzag is large compared to the distance between two vortical structures. Qualitatively, those zigzags are not so different from the ones observed during the free fall of glass spheres in water (**Figure 11*c***). Such path instability has been studied experimentally and theoretically (Horowitz & Williamson 2010) and has been reviewed in Ern et al. (2012). Such instabilities are, however, not supposed to persist for balls, which are typically a hundred times denser than air and move at Reynolds numbers of 10^5. This conclusion seems to be correct as most of the time we observe that balls in sports move straight, as in **Figure 11*a***.

However, if any spherical ball falls from an important height, side deviations are always observed. Darbois-Texier et al. (2013) have conducted such experiments, letting several sport balls fall vertically from a 40-m-high bridge. **Figure 12*a*** presents three examples of recorded trajectories obtained with a Jabulani soccer ball released vertically from rest. Even if the first 10 m are quasi-straight, the end of the fall does exhibit lateral excursions of the order of one ball diameter.

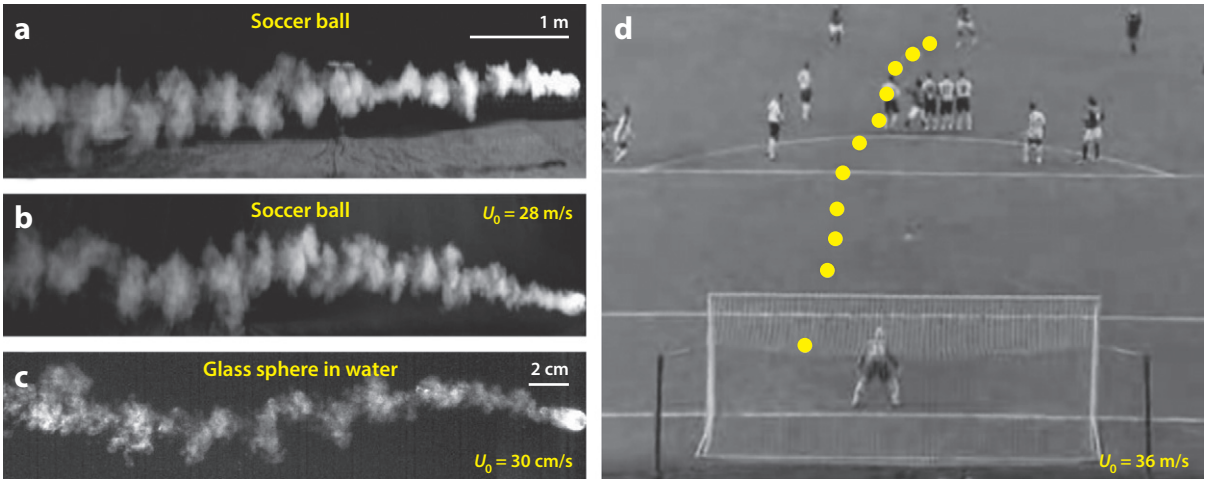

Figure 11

(*a*) Visualization of the straight path of a soccer ball. The white bar stands for 1 m. (*b*) Path of a soccer knuckleball visualized with titanium powder. The velocity is 28 m/s with almost no spin. Panels *a* and *b* reproduced from Hong et al. (2010). (*c*) Free fall of a glass sphere in water (a diameter of 1 cm and a constant velocity of 30 cm/s). In this case, the white bar represents 2 cm, and the whole image has been tilted by 90° for comparison with the soccer ball's path. Panel *c* reproduced with permission from Darbois-Texier (2013). (*d*) A soccer kick taken 33 m from the goal, slightly to the right of center, launched at approximately 36 m/s with one-fourth revolution per second of sidespin from an English Premier League game in 2006. Panel *d* reproduced from Barber et al. (2009).

Such results can be understood using the wind-tunnel measurements of fluctuating aerodynamic forces on spheres reported by Norman & McKeon (2011). This study was performed with a smooth sphere of diameter $D = 15$ cm placed in the 61 cm $\times$ 61 cm $\times$ 244 cm test section of the temperature-controlled recirculating wind tunnel at the California Institute of Technology. The mean velocity U varies from 5 m/s to 50 m/s with a very low free-stream turbulence intensity, $u'/U \leq 0.3\%$. The study is very detailed, and we report here only two results that are essential to understand knuckleballs. Because the sphere is mounted on a force balance, the authors have access to the mean drag coefficients along the direction of the flow ($\bar{C}_x$) and in the transverse directions ($\bar{C}_y$, $\bar{C}_z$). **Figure 12*b*** presents these coefficients as a function of the Reynolds number. Unsurprisingly, the largest force is observed in the direction of the flow with a transition to the supercritical regime at $Re = 3 \times 10^5$. The mean forces in the transverse directions are weak, except in the transition region where they become of the same order as in the direction of the flow. Beside these mean values, the authors also characterize the unsteady forces via the standard deviations $C_i'^2(t) = (C_i(t) - \bar{C}_i)^2$, with the subscript i standing for the direction with respect to the flow ($i = x$ for the flow direction, $i = y$ for horizontal perturbation, and $i = z$ for vertical ones). **Figure 12*c*** shows an example of the dimensionless spectral density of the lateral forces, $\Phi(St)$. The area under the curve is the mean square force fluctuation, $\bar{C}_i'^2 = \int_0^\infty \Phi_i(St) d\,St$, where $St = fD/U$ is the Strouhal number based on the frequency of the perturbation f. The spectral density is shown for two different Reynolds numbers, $Re = 8 \times 10^4$ and $Re = 2.3 \times 10^5$. The classical von Kármán peak at $St = 0.2$ diminishes as the Reynolds number is increased while the level of the low-frequency band increases. The study of Willmarth & Enlow (1969), performed in the supercritical region, revealed that the 0.2 peak is no more visible after the drag crisis. If we reduce the low-band frequency to white noise and study the lateral motion $\delta(t)$ of a ball, we get

$$M \frac{d^2\delta}{dt^2} = \frac{1}{2} \rho U^2 S C_L(f). \tag{16}$$

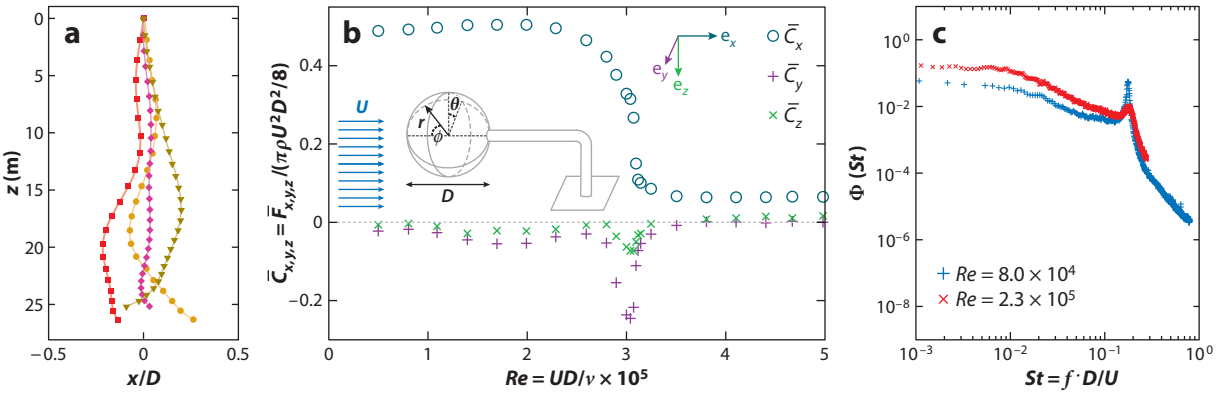

Figure 12

(*a*) Different trajectories of a Jabulani soccer ball released vertically with the same initial conditions ($U_0 = 0$). Along the z direction, the ball accelerates and reaches a Reynolds number of 2.3×10^5 after 25 m. Laterally, erratic excursions of the order of one diameter D are observed. Panel *a* adapted with permission from Darbois-Texier (2013). (*b*) Mean drag coefficients measured on a smooth sphere by Norman & McKeon (2011). (*c*) Normalized power spectral density of the subcritical lateral forces measured on a 15-cm-diameter smooth sphere by Norman & McKeon (2011). The lateral force spectra were averaged. Present results are $Re = 8 \times 10^4$ and $Re = 2.3 \times 10^5$.

Taking $C_L(f) = C_{Lm} \sin(2\pi f t)$ and $\delta = \delta_m \sin(2\pi f t)$, this equation reveals that the frequency for which the amplitude of the deviation δ_m is D is $f = U/(2\pi D)\sqrt{3\rho C_{Lm}/2\rho_s}$. The associated wavelength $\lambda = U/f$ is thus written

$$\frac{\lambda}{D} = 2\pi\sqrt{\frac{2}{3}\frac{\rho_s}{\rho}\frac{1}{C_{Lm}}}. \tag{17}$$

The denser the sphere relative to the fluid, the longer is the zigzag. The larger the lift coefficient, the smaller is the wavelength of the zigzag.

In conclusion, zigzags always exist, but they are only visible if we observe the path of the ball over a distance that is larger than λ. For shorter distances, the lateral deviation is small compared to the diameter, and the zigzag cannot be observed.

A poor man's approach of the knuckleball is as follows: Because **Figure 12*b*** reveals that the lift coefficient is very small except in the transition, we imagine that $C_{Lm} = 0$ outside the transition and $C_{Lm} = C_{L0} = 0.2$ in the transition (values extracted from **Figure 12*b***). With such a simplified model, Equation 17 predicts that the size of the zigzag is infinite outside the transition (and thus not observed). In the transition, it can be observed if the distance of observation is larger than λ. In sports, the largest value of the distance of observation is the size of the field, L_{field}. **Table 2** presents λ for different sports and compares it to L_{field}. It also presents the critical Reynolds number, Re_c, for the different sports and compares it to the maximal value of the Reynolds number, $Re_{\max}$, calculated using $U_{\max}$ in **Table 1**. **Figure 13** presents the ratio $Re_{\max}/Re_c$ as a function of the length ratio L_{field}/λ. In this figure, the knuckleball domain is the upper right area. Indeed, from the argument just developed, the ball must cross the drag crisis. Because the ball decelerates during flight, its maximal Reynolds number must be larger than the critical Reynolds number ($Re_{\max}/Re_c \geq 1$). Moreover, to be observed, the zigzag must be smaller than the sports field ($L_{\text{field}}/\lambda \geq 1$). Those conditions are satisfied for volleyball, baseball, softball, cricket, soccer, and golf.

The surprise here is perhaps to find golf in this category. To our knowledge, knuckleballs have not been reported in golf, but considering the efforts dedicated by companies such as Polara to achieve straight paths, we believe that zigzags exist in golf and can be observed.

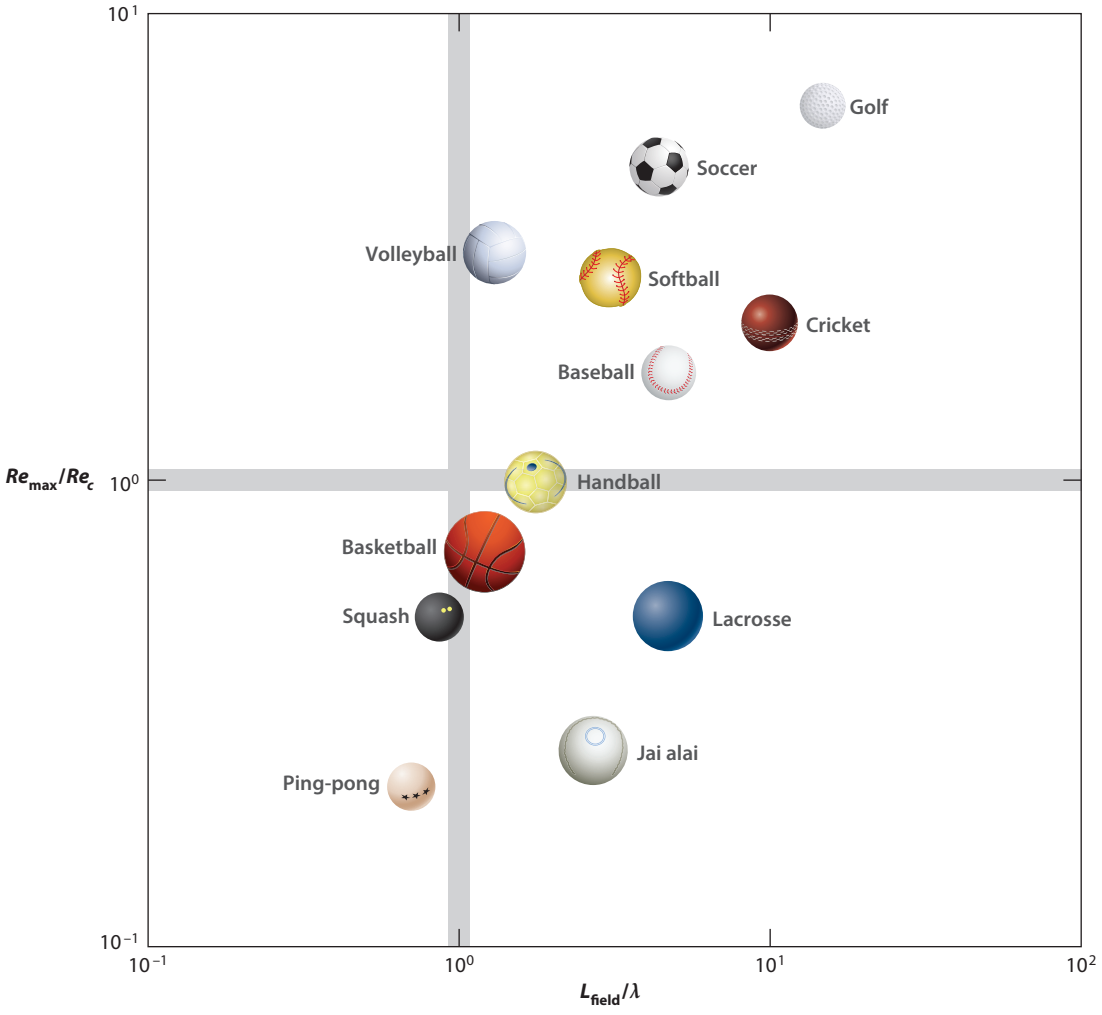

Figure 13

The ratio Re_{max}/Re_c as a function of the length ratio L_{field}/λ. The knuckleball zone exists in the upper right corner.

On the contrary, zigzags cannot be observed in ping-pong (the ball never crosses the transition), squash, lacrosse, jai alai, basketball, and handball. With regard to badminton and tennis, no drag crisis has been reported, and no zigzags have been observed.

Finally, because the drag crisis is sensitive to the roughness of the surface, it is expected that seams will indeed affect the transition. Seams are not required to produce a knuckleball, but they can affect the phenomenon through the velocity at which it is observed and through its amplitude.

3. SHUTTLECOCKS AS A PARADIGM FOR ANISOTROPIC BALLS

In the past decade, the trajectories of shuttlecocks have been studied extensively through experimental, theoretical, and numerical approaches. Cooke (2002) recorded experimental trajectories of different shuttlecocks in the court and compared them with numerical simulations. The

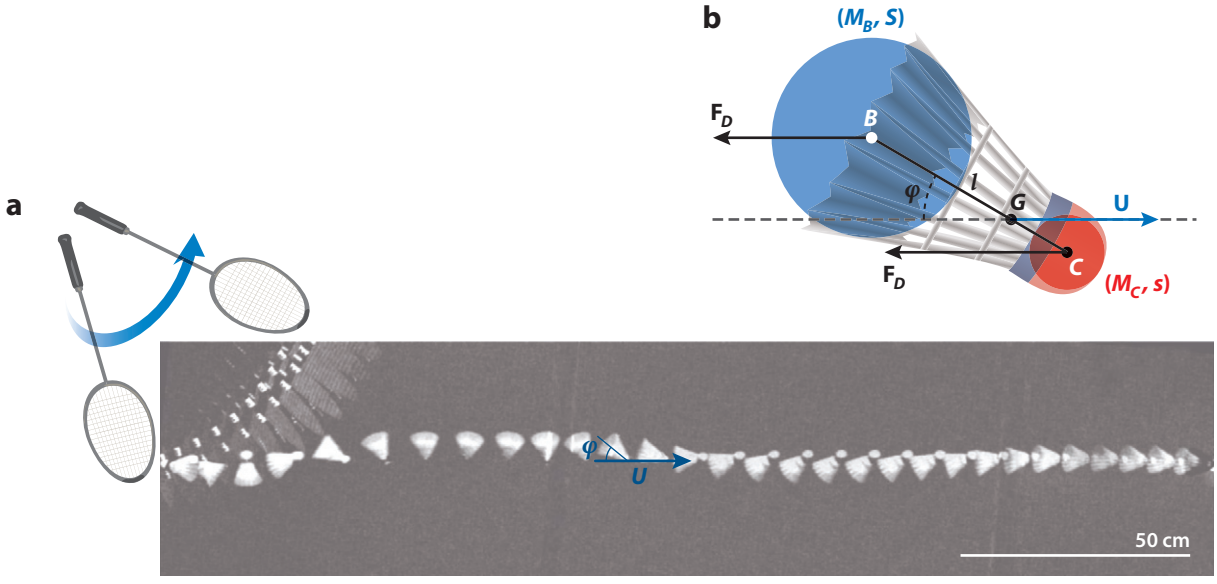

Figure 14

(*a*) Snapshots of a shuttlecock after an impact with a racket. One observes the time evolution of the angle φ between the shuttlecock's orientation and its velocity **U**. White lines indicate 50 cm. The time interval between each position is 5 ms, the shuttlecock's departure velocity is $U_0 \approx 23$ m/s, and its initial angular velocity is $\dot{\varphi}_0 = 206$ rad/s. (*b*) Model of a shuttlecock comprising a sphere of large cross section S and small mass M_B, which represents the skirt, and a sphere of small cross section s and large mass M_C, which represents the cork. Figure reproduced with permission from Cohen et al. (2014b).

aerodynamics of several shuttlecocks has also been inspected in a wind tunnel by Cooke (1999) and Alam et al. (2010). They measured the air drag and showed that the drag coefficient C_D is more approximately constant for Reynolds number ranging from 10^4 to 2×10^5. For commercial shuttlecocks, the drag coefficient varies between 0.6 and 0.7 depending on the model. Wind-tunnel measurements also reveal that there is no lift force on a shuttlecock when its axis of symmetry is aligned with its velocity direction. A synthesis of data collected in the court and in a wind tunnel has been done by Chan & Rossmann (2012).

The cylindrical symmetry that characterizes a shuttlecock allows it to flip, that is, to change direction after impact. **Figure 14*a*** illustrates this effect in which the flip lasts three time intervals, which corresponds to 15 ms. The oscillating time of the shuttlecock direction is estimated to be 80 ms. After 130 ms, the shuttlecock axis of symmetry is aligned with its velocity direction.

To understand this complex dynamic, we must evaluate the forces applied to it, namely the weight and aerodynamic forces. The latter reduces to a drag force, the application point of which is the pressure center where aerodynamic torque vanishes (Etkin & du Reid 1982). Because the mass repartition is nonhomogeneous in a shuttlecock, its center of gravity is closest to the cork and differs from the center of pressure. Using numerical simulations, Cooke (2002) estimated that the distance between the center of mass and center of pressure of a shuttlecock is approximately 3.0 cm. **Figure 14*b*** highlights the effect of the aerodynamic drag, $\mathbf{F}_D$, on an inclined shuttlecock. When the shuttlecock moves to the right, the aerodynamic drag $\mathbf{F}_D$ is oriented to the left and exerts a torque counterclockwise, which brings the shuttlecock back on the axis ($\varphi = 0$). However, when the shuttlecock moves to the left, as is the case after impact, the aerodynamic drag $\mathbf{F}_D$ is oriented to the right, and the aerodynamic torque acts clockwise, stabilizing the shuttlecock in the

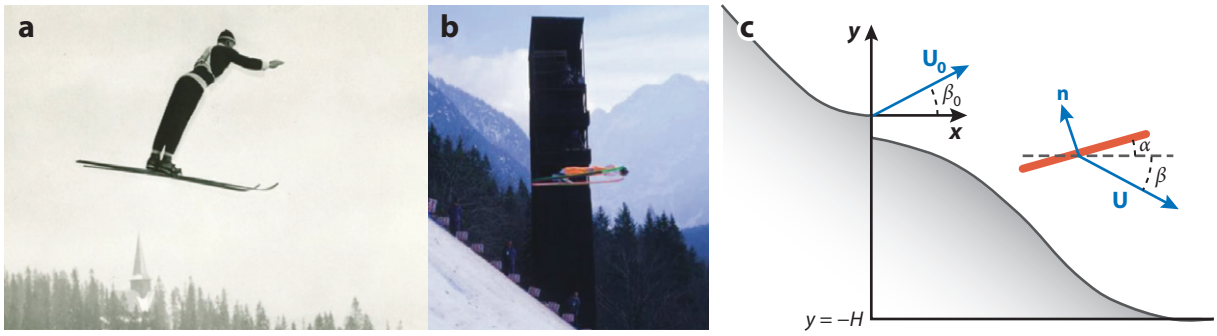

Figure 15

(*a*) The Kongsberger technique, a style of ski jumping developed in the early 1920s by Jacob Tullin Thams and Sigmund Ruud. (*b*) C. Duffner (Germany) on a ski flying hill in Planica, Slovenia, in 1994. Panel *b* courtesy of W. Müller. (*c*) Conventions used to describe ski-jump flight.

position $\varphi = \pi$. Owing to this aerodynamic torque, each player is thus able to hit the cock and not the skirt.

Because the versatile behavior of a shuttlecock originates from the distinction between its center of mass and center of pressure, we model this object with two spheres, one for the skirt with a small mass M_B and a large cross section S positioned in B and the second representing the cork with a larger mass M_C and a small cross section s positioned in C (**Figure 14*b***). The shuttlecock is thus reduced to a heavy small cork and a large light skirt. A torque balance around G provides the following equation in the limit $S \cdot M_C \gg s \cdot M_B$:

$$\ddot{\varphi} + \frac{\rho S C_D U_0}{2M_B(1 + M_B/M_C)}\dot{\varphi} + \frac{\rho S C_D U_0^2}{2(M_C + M_B)l_{GC}} \sin\varphi = 0, \tag{18}$$

where C_D is the drag coefficient of a sphere, and l_{GC} is the distance between the points G and C ($l_{GC} = M_B/M_C l_{BC}$). The calculation leading to Equation 18 has been detailed in Cohen et al. (2014b). This second-order differential equation for φ corresponds to a damped oscillator. The square of pulsation, $\omega_0^2 = \rho S C_D U_0^2/2M l_{GC}$, is linked to the stabilizing torque generated by the aerodynamic drag. The damping term, $1/\tau_s = \rho S C_D U_0/2M_B(1 + M_B/M_C)$, results from the drag associated with the orthoradial movement of the shuttlecock as φ varies. Using the values corresponding to **Figure 14*a*** with $M_B = 2$ g, $M_C = 3$ g, $l_{GC} = 2$ cm, $C_D = 0.6$, and $S \approx 28$ cm^2, we get $2\pi/\omega_0 \approx 90$ ms for the period of oscillation and $\tau_d \approx 140$ ms for the damping time. Both values are compatible with the observations.

4. THE SKI JUMP AND THE (ALMOST) NO-SYMMETRY LIMIT

The ski-jumping technique has changed several times over the years from an almost vertical position (**Figure 15*a***) to a horizontal one (**Figure 15*b***) (Müller 2008b). We discuss this evolution using the conventions presented in **Figure 15*c***.

Reducing the ski jumper to a flat plate (mass M, surface S) enables one to write the equation of the jump flight as (Carmigniani et al. 2013)

$$M\frac{d\mathbf{U}}{dt} = M\mathbf{g} + \frac{1}{2}\rho U^2 S C_D \sin(\alpha - \beta)\mathbf{n}. \tag{19}$$

This equation must be solved with the initial conditions $\mathbf{U}(t = 0) = \mathbf{U}_0$. Compared to a sphere, the direction of the aerodynamic force now depends on the geometry. For a flat plate, this force is normal to the plate (Hoerner 1965). In the small-angle limit, $\alpha \ll 1$, the normal is almost

aligned with the vertical ($\mathbf{n} \cdot \mathbf{e}_x \approx 0$), and Equation 19 reduces in the $\mathbf{e}_x$ direction to $dU_x/dt = 0$, from which we obviously get $x = U_0 \cos\beta_0 t$. Along the $\mathbf{e}_y$ direction, Equation 19 reduces to $dU_y/dt = -g - \rho S C_D \cos\alpha U U_y/2M$. Following the studies of Müller et al. (1995) and Müller (2008a), it appears that the velocity U weakly changes between takeoff and landing, maintaining a value close to 30 m/s. The condition $U \approx U_0$ allows one to integrate the equation and get the approximate trajectory:

$$\frac{gy}{U_0^2} = -\frac{gx}{U_0^2}\frac{1}{D_r \cos\alpha \cos\beta_0} + \frac{1 + D_r \cos\alpha \sin\beta_0}{(D_r \cos\alpha)^2}\left[1 - e^{-\frac{gx}{U_0^2}\frac{D_r \cos\alpha}{\cos\beta_0}}\right], \quad (20)$$

where $D_r = \rho U_0^2 S C_D/2Mg$ is the drag to weight ratio. In the limit of small drag ($D_r \ll 1$), the trajectory in Equation 20 reduces to the parabolic flight in Equation 5. In the opposite limit of a perfect flyer ($D_r \gg 1$), the trajectory in Equation 20 allows one to predict the jump length at a fixed location $y = -H$:

$$x(y = -H) \approx H \cdot D_r \cos\alpha \cdot \cos\beta_0. \quad (21)$$

This expression reveals that the length of the jump is maximized for large values of D_r and for $\cos\alpha = 1$ and $\cos\beta_0 = 1$. For athletes, one way to increase D_r is to decrease their mass ($\lim_{M\to 0} D_r = \infty$). This effect did have major consequences for ski jumpers in the sense that some became anorexic (Schmölzer & Müller 2002). The condition $\cos\alpha = 1$ allows us to understand the horizontal position observed in **Figure 15*b***. Finally, the condition $\cos\beta_0 = 1$ also allows us to understand the large effort by athletes to increase their vertical velocity at takeoff (Virmavirta et al. 2009). Indeed, the in-run track makes a $-10°$ angle with the horizontal direction. To get close to the condition $\beta_0 = 0$, an athlete must reach a vertical velocity of $U_{y0} = U_0 \sin(10) \approx 5.2$ m/s. This value is compatible with measurements performed at takeoff by Virmavirta et al. (2009) and Müller (2013). The model just discussed is obviously too basic to account for the complexity of the whole phenomenon, and more detailed approaches can be found in Schmölzer & Müller (2005).

Above we discuss the trajectory of the center of mass assuming that the jumper is able to keep a constant angle α. **Figure 16*a*** presents what would happen after takeoff (top left corner)

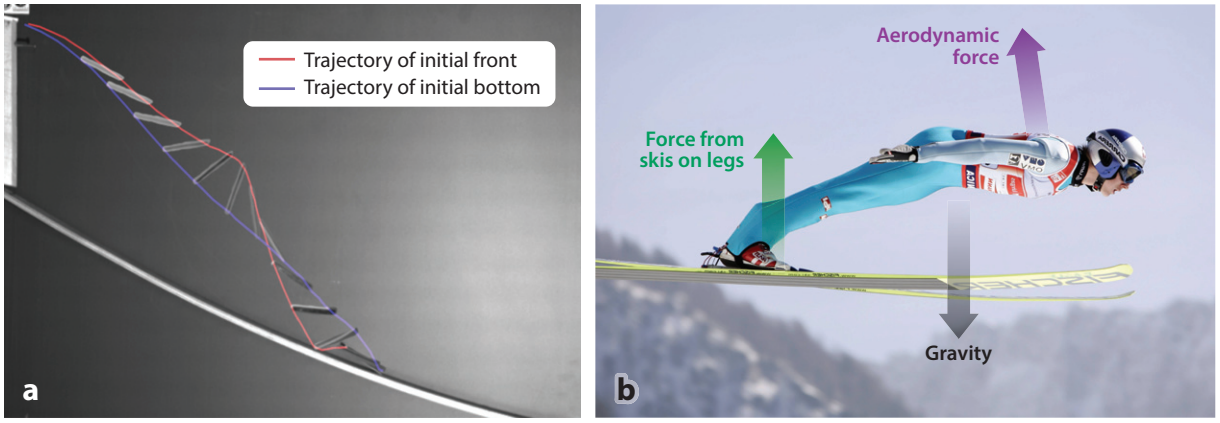

Figure 16

(*a*) A plate (metro ticket) taking off on a ramp with a final slope of $-10°$ (top left corner). The plate is falling toward the bottom right corner and tumbles while falling. The images are separated by 20 ms. The red line is the trajectory of the initial front part of the plate, and the blue line follows the initial bottom part of it. (*b*) Ski-jumper stability. The gray arrow represents the gravity field force, the purple arrow is the aerodynamic force described in Equation 19, and the green arrow is the force exerted by the skis on the jumper's legs. Figure adapted with permission from Carmigniani et al. (2013).

if the jumper were really behaving as a flat plate. Because the aerodynamic force applies at the aerodynamic center, which is close to the leading edge for a plate, the aerodynamic force exerts a torque on the plate that makes it rotate counterclockwise. To avoid this tumbling instability (Mahadevanand et al. 1996, Andersen et al. 2005), the ski jumper balances the aerodynamic force acting on his or her body by the aerodynamic force acting on the skis (**Figure 16*b***). Although not presented in the figure, the arms also help the jumper to achieve stability (Marques-Bruna & Grimshaw 2009a,b).

5. CONCLUSION

Aerodynamics plays a major role in the trajectory of sports projectiles, and above we have tried to discuss some of its salient features. We do not pretend to be exhaustive, and this is perhaps a good place, in the conclusion, to underline some questions that have not been addressed.

Among those sports absent, one could mention rugby or American football, which are played with oval balls. With spin and gyroscopic stabilization, these balls should behave almost like a ski jumper, in the sense of keeping a constant angle and feeling a force that depends on its orientation. However, without spin, the complexity of the trajectory is increased (Seo et al. 2008) and probably deserves some further study.

Apart from rugby and American football, the more noticeable sports missing from the review are throwing sports, such as those involving the shot put, javelin, and discus. The shot put is probably the easiest of the three in terms of its trajectory because it belongs to the gravitational family in which parabolae are the rule. The javelin and discus are more subtle in the sense that their positions during flight result from a fluid-structure interaction problem. In that sense, they could be viewed as a prolongation of the ski-jumper problem in which the constraint of constant angle has been relaxed. Focusing on the javelin, these particles represent a good challenge in the sense that they incline and vibrate along their trajectory. Looking for the optimal design that maximizes the range is a well-posed (complex) problem.

DISCLOSURE STATEMENT

The author is not aware of any biases that might be perceived as affecting the objectivity of this review.

ACKNOWLEDGMENTS

I would like to thank here all the people who have made this review possible. Among them, two wonderful PhD students, Caroline Cohen and Baptiste Darbois-Texier, have jointly conducted studies on badminton, the size of sports fields, and knuckleballs, always with amazing scientific skills and a huge joy of living. Along with their research, they also co-organized the Euromech Conference on the Physics of Sports, which allowed us to meet with Alan Nathan and discuss his work on pop-ups and knuckleballs and also meet with Wolfram Müller and discuss his huge contribution to ski jumping. J.W.M. Bush also attended the conference and produced one of the best articles I know on soccer trajectories. Research discussed in this review has been conducted since 2007 in the Soft Matter group both at ESPCI and at Ecole Polytechnique in collaboration with David Quéré. His enthusiasm, taste, and exigency in research motivate the whole group on a daily basis, and it is a deep pleasure to thank him here. All the members of the group and LadHyX as a whole must also be thanked. The physics of sports is not (by far) a traditional topic of the lab. It is, however, the lab's tradition to let people develop their own research, and I deeply thank the

whole lab for respecting this tradition. Outside the lab, I sincerely thank E. Reyssat, M. Rabaud, P. Gondret, J.P. Hulin, M. Fermigier, and E. Guyon for their attentive reading of the original version of the article and their constructive comments. Finally, this review would not have existed without Elisabeth Guazzelli, who proposed it to me two years ago. May all of them find in these few lines the expression of my sincere gratitude.

LITERATURE CITED

Alam F, Chowdhury H, Theppadungporn C, Subic A. 2010. Measurements of aerodynamic properties of badminton shuttlecocks. *Procedia Eng.* 2:2487–92

Alam F, Ho H, Smith L, Subic A, Chowdhury H, Kumar A. 2012. A study of baseball and softball aerodynamics. *Procedia Eng.* 34:86–91

Andersen A, Pesavento U, Wang J. 2005. Analysis of transitions between fluttering, tumbling and steady descent of falling cards. *J. Fluid Mech.* 541:91–104

Asai T, Kamemoto K. 2011. Flow structure of knuckling effect in footballs. *J. Fluids Struct.* 27:727–33

Asai T, Seo K, Kobayashi O, Sakashita R. 2007. Fundamental aerodynamics of the soccer ball. *Sports Eng.* 10:101–10

Barber S, Chin S, Carré M. 2009. Sports ball aerodynamics: a numerical study of the erratic motion of soccer balls. *Comput. Fluids* 38:1091–100

Bush J. 2013. The aerodynamics of the beautiful game. See Clanet 2013, pp. 171–92

Carmigniani R, Cao X, Savourey S, Martinier C, Nuytten S, et al. 2013. Ski jump flight. See Clanet 2013, pp. 286–301

Chan C, Rossmann J. 2012. Badminton shuttlecock aerodynamics: synthesizing experiment and theory. *Sports Eng.* 15:61–71

Cho A. 2004. Engineering of sport. *Science* 306:42–43

Chudinov P. 2010. Approximate formula for the vertical asymptote of projectile motion in midair. *Int. J. Math. Educ. Sci. Technol.* 41:92–98

Clanet C, ed. 2013. *Sports Physics*. Palaiseau, Fr.: Ed. Ecole Polytech.

Cohen C, Darbois-Texier B, Dupeux G, Brunel E, Quéré D, Clanet C. 2014a. The aerodynamical wall. *Proc. R. Soc. Lond. A* 470:20130497

Cohen C, Darbois-Texier B, Quéré D, Clanet C. 2014b. Physics of badminton. *New J. Phys.* In press

Cooke A. 1999. Shuttlecock aerodynamics. *Sports Eng.* 2:85–96

Cooke A. 2002. Computer simulation of shuttlecock trajectories. *Sport Eng.* 5:93–105

Cottey R. 2002. *The modelling of spin generation with particular emphasis on racket ball games*. PhD Thesis, Loughborough Univ.

Darbois-Texier B. 2013. *Tartaglia, zigzag and flips: les particules denses à haut Reynolds*. PhD Thesis, Univ. Paris Diderot

Darbois-Texier B, Cohen C, Dupeux G, Quéré D, Clanet C. 2014. On the size of sports fields. *New J. Phys.* 16:033039

Darbois-Texier B, Cohen C, Quéré D, Clanet C. 2013. Knuckleballs. See Clanet 2013, pp. 199–212

de Mestre N. 1990. *The Mathematics of Projectiles in Sport*. Cambridge, UK: Cambridge Univ. Press

Deprá P, Brenzikofer R, Goes M, Barros R. 1998. Fluid mechanics analysis in volleyball services. *16 Int. Symp. Biomech. Sports.* Int. Soc. Biomech. Sports. **https://ojs.ub.uni-konstanz.de/cpa/article/view/1602**

Drake S. 1973. Galileo's experimental confirmation of horizontal inertia: unpublished manuscripts. *Isis* 64:291–305

Dupeux G, Cohen C, Goff AL, Quéré D, Clanet C. 2011. Football curves. *J. Fluids Struct.* 27:659–67

Dupeux G, Goff AL, Quéré D, Clanet C. 2010. The spinning ball spiral. *New J. Phys.* 12:093004

eFastball.com. 2011. *Bat speed, batted ball speed (exit speed) in MPH by age group*. **http://www.efastball.com/hitting/average-bat-speed-exit-speed-by-age-group/**

Erlichson H. 1983. Maximum projectile range with drag and lift, with particular application to golf. *Am. J. Phys.* 51:357–62

Ern P, Risso F, Fabre D, Magnaudet J. 2012. Wake-induced oscillatory paths of bodies freely rising or falling in fluids. *Annu. Rev. Fluid Mech.* 44:97–121
Etkin B, du Reid L. 1982. *Dynamics of Flight: Stability and Control*. New York: Wiley
Frohlich C. 2011. Resource letter PS-2: physics of sports. *Am. J. Phys.* 79:565–74
Galilei G. 1638. *Dialogues Concerning Two New Sciences*. Leiden: L. Elzevier
Gillmeister H. 1998. *Tennis: A Cultural History*. New York: New York Univ. Press
Gorostiaga E, Granados C, Ibanez J, Izquierdo M. 2005. Differences in physical fitness and throwing velocity among elite and amateur male handball players. *Int. J. Sports Med.* 26:225–32
Greenwald R, Penna L, Crisco J. 2001. Differences in batted ball speed with wood and aluminum baseball bats: a batting cage study. *J. Appl. Biomech.* 17:241–52
Häyrinen M, Lahtinen P, Mikkola T, Honkanen P, Paananen A, Blomqvist M. 2007. *Serve speed analysis in men's volleyball*. Presented at Science for Success II, Jyvaskyla, Finl.
Higuchi H, Kiura T. 2012. Aerodynamics of knuckleball: flow-structure interaction problem on a pitched baseball without spin. *J. Fluids Struct.* 32:65–77
Hoerner SF. 1965. *Fluid-Dynamic Drag*. Bricktown, NJ: Hoerner Fluid Dyn.
Hong S, Chung C, Nakayama M, Asai T. 2010. Unsteady aerodynamic force on a knuckleball in soccer. *Procedia Eng.* 2:2455–60
Horowitz M, Williamson CHK. 2010. The effect of Reynolds number on the dynamics and wakes of freely rising and falling spheres. *J. Fluid Mech.* 651:251–94
Huston R, Cesar A. 2003. Basketball shooting strategies: the free throw, direct shot and layup. *Sports Eng.* 6:49–64
Keller J. 1974. Optimal velocity in a race. *Am. Math. Mon.* 81:474–80
Lamb H. 1914. *Dynamics*. Cambridge, UK: Cambridge Univ. Press
MacKenzie S, Kortegaard K, LeVangie M, Barro B. 2012. Evaluation of two methods of the jump float serve in volleyball. *J. Appl. Biomech.* 28:579–86
Mahadevanand L, Ryu W, Adt S. 1996. Tumbling cards. *Phys. Fluids* 11:1–3
Marques-Bruna P, Grimshaw P. 2009a. Mechanics of flight in ski jumping: aerodynamic stability in pitch. *Sports Technol.* 2:24–31
Marques-Bruna P, Grimshaw P. 2009b. Mechanics of flight in ski jumping: aerodynamic stability in roll and yaw. *Sports Technol.* 2:111–20
McBeath MK, Nathan AM, Bahill AT, Baldwin DG. 2008. Paradoxical pop-ups: Why are they difficult to catch? *Am. J. Phys.* 76:723–29
Mehta D. 1985. Aerodynamics of sports balls. *Annu. Rev. Fluid Mech.* 17:151–89
Mehta R. 2008. Sports ball aerodynamics. In *Sport Aerodynamics*, ed. H Norstrud, pp. 229–331. New York: Springer
Mehta R, Alam F, Subic A. 2008. Aerodynamics of tennis balls: a review. *Sports Technol.* 1:1–10
Mehta R, Pallis J. 2001. Sports ball aerodynamics: effects of velocity, spin and surface roughness. In *Materials and Science in Sports*, ed. S Froes, S Haake, pp. 185–97. Warrendale, PA: TMS
Müller W. 2008a. Computer simulation of ski jumping based on wind tunnel data. *Sport Aerodyn.* 506:161–82
Müller W. 2008b. Performance factors in ski jumping. *Sport Aerodyn.* 506:139–60
Müller W. 2013. Physics of ski jumping. See Clanet 2013, pp. 271–86
Müller W, Platzer D, Schmölzer B. 1995. Scientific approach to ski safety. *Nature* 375:455
Nathan AM. 2003. Characterizing the performance of baseball bats. *Am. J. Phys.* 71:134–43
Nathan AM. 2008. The effect of spin on the flight of a baseball. *Am. J. Phys.* 76:119–24
Nathan AM. 2012. Analysis of knuckleball trajectories. *Procedia Eng.* 34:116–21
Newton I. 1671. New theory about light and colors. *Philos. Trans.* 6:3075–87
Norman A, McKeon B. 2011. Unsteady force measurements in sphere flow from subcritical to supercritical Reynolds numbers. *Exp. Fluids* 51:1439–53
Rayleigh L. 1877. On the irregular flight of a tennis ball. *Messenger Math.* 7:14–16
Reep C, Benjamin B. 1968. Skill and chance in association football. *J. R. Stat. Soc. A* 131:581–85
RIA Novosti. 2013. Malaysian badminton star breaks smash speed record. *RIA Novosti*, Aug. 23. **http://en.ria.ru/sports/20130823/182930446.html**

Russell DA. 2008. *Explaining the 98-mph BBS standard for ASA softball*. **http://www.acs.psu.edu/drussell/bats/bbs-asa.html**

Schmölzer B, Müller W. 2002. The importance of being light: aerodynamic forces and weight in ski jumping. *J. Biomech.* 35:1059–69

Schmölzer B, Müller W. 2005. Individual flight styles in ski jumping: results obtained during Olympic Games competitions. *J. Biomech.* 38:1055–65

Seo K, Kobayashi O, Murakami M. 2008. The fluctuating flight trajectory of a non-spinning punted ball in rugby. *Eng. Sport* 7:329–36

Sheppard D. 2013. Tracking R.A. Dickey's knuckleball. *FanGraphs*, June 18. **http://www.fangraphs.com/blogs/tracking-r-a-dickeys-knuckleball/**

Tartaglia N. 1537. *Nova Scientia*. Venice: Stefano dei Nicolini da Sabbio

Truscott TT, Techet AH. 2009. Water entry of spinning spheres. *J. Fluid Mech.* 625:135–65

Turberville J. 2003. *Table tennis ball speed*. **http://www.jayandwanda.com/tt/speed.html**

Virmavirta M, Isolehto J, Komi P, Schwameder H, Pigozzi F, Massazza G. 2009. Take-off analysis of the Olympic ski jumping competition (HS-106m). *J. Biomech.* 42:1095–101

Volleywood. 2012. Matey & Santos' lightning spikes. *Volleywood*, May 8. **http://www.volleywood.net/volleyball-related-news/volleyball-news-north-america/kaziyski-santos-lightning-spikes/**

Willmarth W, Enlow RL. 1969. Aerodynamic lift and moment fluctuations of a sphere. *J. Fluid Mech.* 36:417–32